

# Section 1

## PROGRESS IN LASER FUSION

### 1.A Theoretical Interpretation of OMEGA Glass-Ablator Cryogenic Implosion Experiments

Simulations of direct-drive, high-gain capsule designs have shown that thick, frozen-DT-fuel layers and low-atomic-number ablators are requirements for optimal performance. However, current target-fabrication and handling limitations preclude the use of energy-scaled capsules of this type in current direct-drive experiments. The only targets now available that are capable of providing moderately thick, frozen fuel layers are high-pressure ( $P_0 \geq 100$  atm), DT-filled glass microballoons. A series of direct-drive laser-fusion experiments using DT-filled cryogenically cooled glass-ablator capsules has been performed on the OMEGA 24-beam, 351-nm laser system.<sup>1,2</sup> These experiments, which represent a first attempt at studying the hydrodynamic behavior of cryogenic-fuel-layer capsules on OMEGA, resulted in the highest directly measured fuel areal densities ( $\rho R_f$ ) achieved to date using the direct-drive approach to inertial confinement fusion. However, significant departures from predicted one-dimensional (1-D) performance with respect to both neutron yield and  $\rho R_f$  were observed.

In this article we present our latest understanding of the observed discrepancies. In the first section we briefly review the experimental conditions, experimental results, and the simulation methodology used in modeling these experiments. In the remaining sections we discuss possible causes for the departures from 1-D performance. We show that, based on our latest understanding, there is a potential for a classically Rayleigh-Taylor<sup>3-5</sup> unstable interface to develop within the DT-fuel layer during the

acceleration phase of the implosion, which we believe is the principal cause for the discrepancies between experiment and simulation.

### Experiments and Results

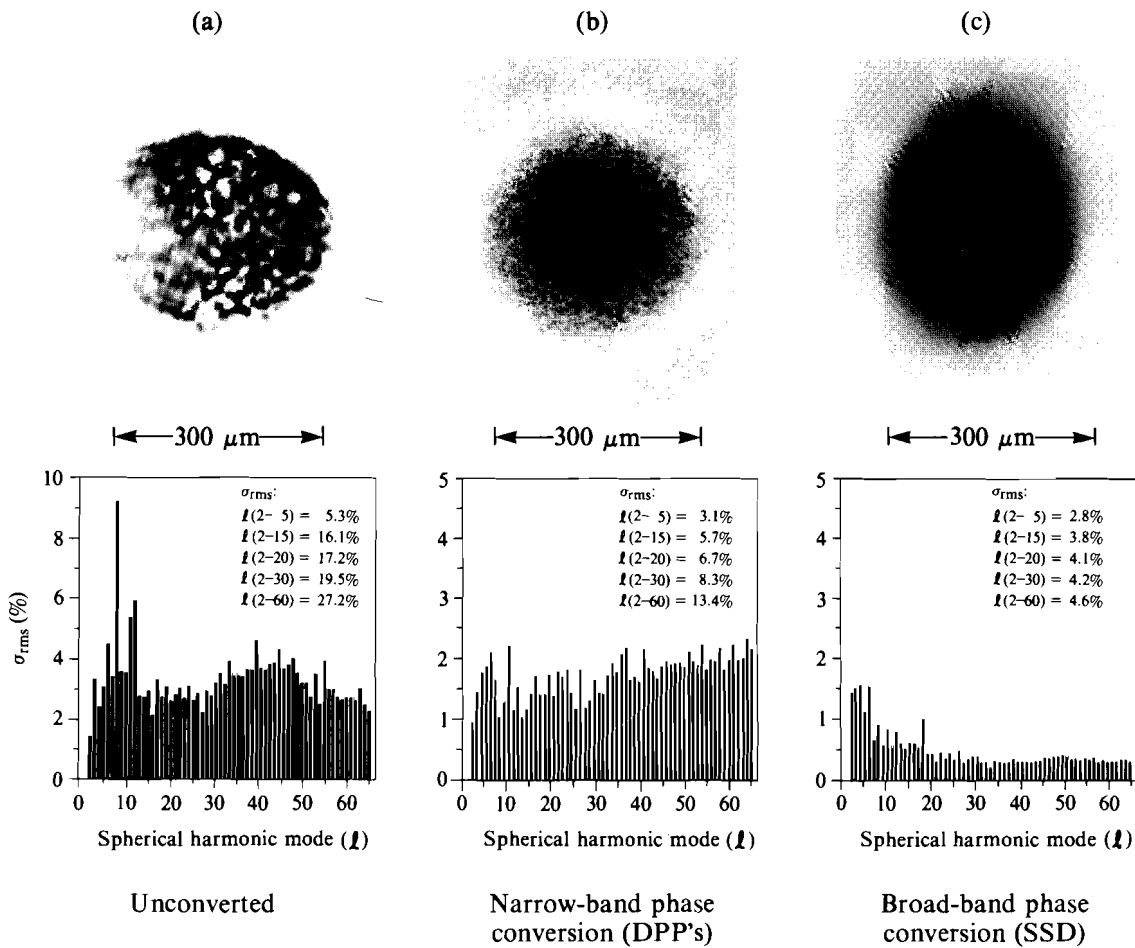
Glass microballoons containing approximately equimolar mixtures of D and T at densities corresponding to 75- and 100-atm, room-temperature fill pressures were used in these experiments. (In this article we will restrict our discussion to the 100-atm fill implosion results only.) The target inner diameters were  $\sim 250 \mu\text{m}$  and the glass-ablator thicknesses varied between 3 and  $10 \mu\text{m}$ . The targets were supported (using no glue) by four or five spider silks approximately  $0.5 \mu\text{m}$  in diameter drawn across a copper U-shaped mount. The width and thickness of the copper mounts were constrained by the requirements that the mount fit in the liquid-He-cooled shroud and that it not obscure any OMEGA laser beams.<sup>1</sup> To provide additional mechanical stability, the mount assembly, including the target, was coated with  $0.2 \mu\text{m}$  of parylene. A detailed description of the cryogenic-target cooling and positioning system used in these experiments is given in Ref. 1.

The capsules were irradiated with up to 1500 J of 351-nm laser light. The pulse shapes were approximately Gaussian with full-width-half-maxima (FWHM) in the 600-ps to 650-ps range. The cryogenic implosion experiments presented in this article were conducted using two (theoretically calculated) different on-target illumination conditions. The first series incorporated the use of a distributed phase plate<sup>6</sup> (DPP) in each beam of the OMEGA laser system before the final focus lens. The second series, performed six months later, involved the initial implementation of a new method to improve on-target illumination uniformity compatible with frequency-tripled glass laser systems [smoothing by spectral dispersion (SSD)].<sup>7</sup> The predicted levels of illumination nonuniformity for these two series of experiments are shown in Fig. 43.1.

Numerical simulations of the cryogenic implosion experiments were performed using the one- and two-dimensional hydrodynamic codes *LILAC* and *ORCHID*. Both codes contain Lagrangian hydrodynamics, a tabular equation of state (SESAME),<sup>8</sup> thermonuclear burn, multigroup fusion reaction particle transport, and multifrequency radiation transport. The opacities used in the multifrequency radiation transport are obtained by reducing the Los Alamos National Laboratory 2000-frequency-group, local thermodynamic equilibrium library<sup>9</sup> to a desired group structure. Laser energy deposition is modeled using a geometric optic<sup>10</sup> ray-trace algorithm with energy deposited by inverse bremsstrahlung along each ray path. Flux limitation<sup>11</sup> of the Spitzer-Härm electron thermal transport is incorporated as a “sharp cutoff.”

Simulations of the actual implosion experiments were performed using the measured values of capsule dimensions, room-temperature fill pressures, incident laser energy, and laser pulse width. Measurements of the cryogenic-fuel-layer thickness, temperature, and residual vapor gas density were not

obtained during these experiments. However, the temperature of the cooling shroud was measured and was typically in the range between 6°K and 8°K. By assuming that the capsule and the shroud were near thermal equilibrium (turbulent gaseous helium providing the path for heat conduction), the capsule frozen-fuel-layer conditions could be inferred. (For the simulations presented in this article, an initial DT-solid-fuel density of 0.26 g/cm<sup>3</sup> was used.<sup>12</sup>)



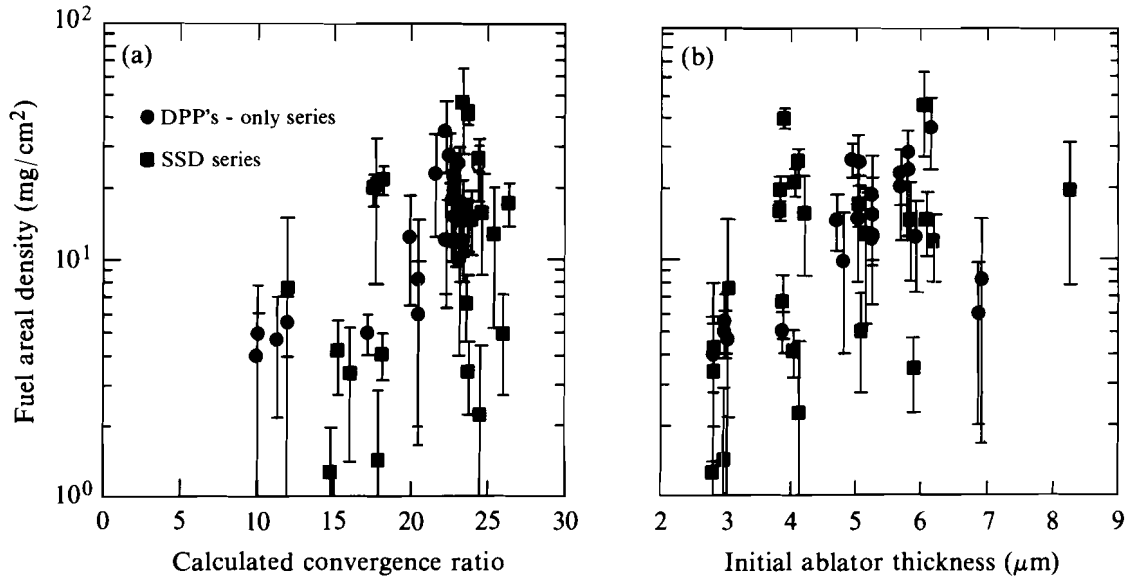
E5267

Fig. 43.1  
Equivalent-target-plane distribution measured on one OMEGA beamline: (a) without DPP's, (b) with DPP's, (c) with SSD. The corresponding spherical-harmonic decompositions of overall uniformity on target, assuming 1% thermal smoothing, are shown underneath. Note the different scale on the bottom-left figure.

The density of the residual vapor gas at temperatures ≤ 8°K is extremely small<sup>12</sup> and was therefore neglected in the simulations presented here. However, this raises questions regarding the numerical treatment of the

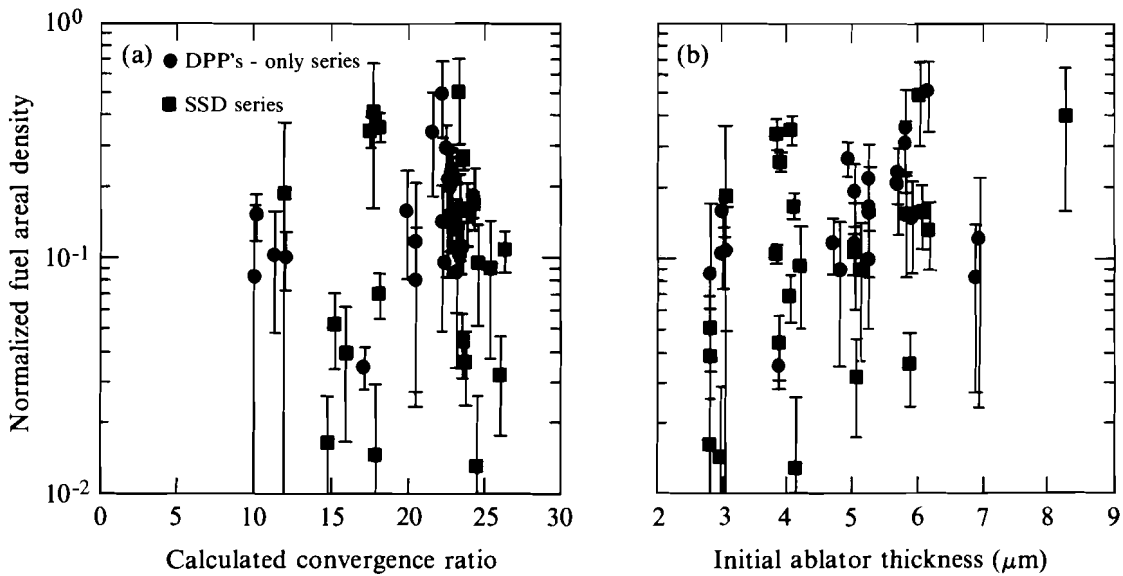
void closure during the simulation and its potential influence on the predicted neutron production and capsule compression. One-dimensional simulations conducted for this study have shown that for a vast majority of the implosions modeled, the ion mean free path associated with the heating of the central fuel region at the time of void closure is short when compared to the size of the first fuel zone. Therefore, for the numerical results presented here, the kinetic energy associated with the inner fuel zone boundary is deposited into the ions of the first fuel zone at the time of void closure. To examine the sensitivity of this choice, 1-D calculations were conducted in which the kinetic energy of the inner fuel boundary was distributed over a number of inner fuel zones. These calculations showed a small yield reduction (less than a factor of 2) and a slight increase in the final neutron-weighted fuel and shell areal density when compared to the same cases in which the first zone dump of the kinetic energy was used. Simulations were also performed in which the residual vapor was modeled thereby avoiding the issues associated with void closure. Results from these calculations showed a small neutron-yield increase (approximately a factor of 2) and a slight decrease in the neutron-weighted areal densities when compared to the first zone kinetic-energy dump cases. Since the numerical simulations presented in the remaining sections were carried out in a similar manner we do not expect the issues associated with void closure to affect the interpretation of the trends in the experimental data; however, it could affect absolute comparisons for a particular simulation/shot.

The measured fuel areal density (neutron averaged) versus calculated convergence ratio and initial ablator thickness is shown in Figs. 43.2(a) and 43.2(b) respectively. The measured fuel-areal-density values were obtained using the “knock-on” diagnostic.<sup>13–15</sup> This diagnostic measures the number of deuterons and tritons in the compressed fuel elastically scattered by the 14.1-MeV neutrons emitted from the DT fusion reactions. The number of scattered “knock-on” ions is directly proportional to the fuel areal density. The possible presence of fuel-ablator mixing during neutron emission, while affecting the overall implosion dynamics, has little effect on the interpretation of the fuel areal density since only the elastically scattered fuel deuterons and tritons are measured. However, the areal-density value obtained does depend on the spatial extent of the neutron emission, which can be influenced by the presence of mixing during the stagnation phase of the implosion. [For example, for the same uniform (radial) fuel-density profile, a case in which the neutron emission was uniform throughout the fuel region would result in an inferred fuel areal density 4/3 higher than a case in which the neutron emission was from a central point source. In the cases presented here we have assumed that the neutron emission was from a central point source when determining  $\rho R_f$ .] The normalized fuel  $\rho R_f$  (measured  $\rho R_f$  / 1-D neutron-averaged fuel  $\rho R$ ) versus calculated convergence ratio and initial ablator thickness is displayed in Fig. 43.3(a) and 43.3(b). The calculated convergence ratio is defined as the initial fuel-ablator interface radius divided by the minimum radius of this interface during the implosion.



TC2785

Fig. 43.2  
Fuel areal density versus (a) calculated convergence ratio and (b) initial ablator thickness.



TC2786

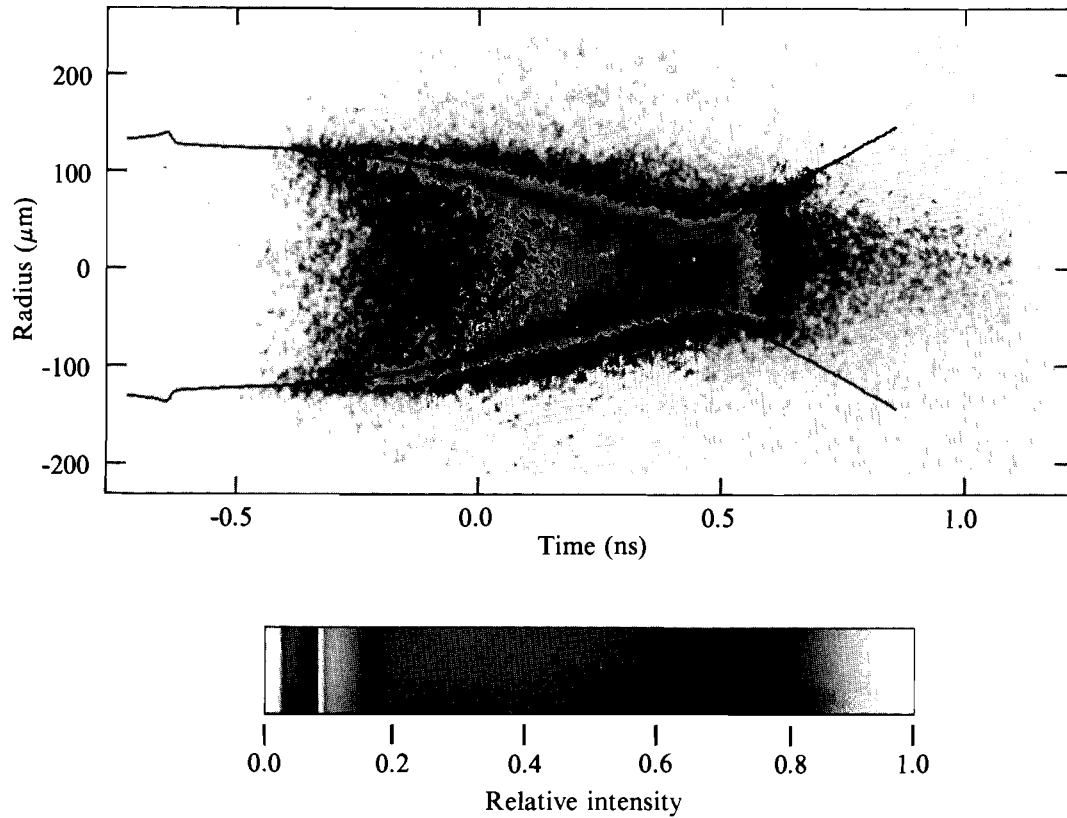
Fig. 43.3  
Normalized fuel areal density versus (a) calculated convergence ratio and (b) initial ablator thickness.

Figure 43.3 shows that, for those data points with reasonable statistical uncertainty, the measured fuel areal density ranges between a factor of 2 to 50 below code predictions. The observed neutron yield obtained for these implosions ranged between  $10^{-3}$  and  $10^{-4}$  of the simulated 1-D neutron yield. In the following sections we attempt to identify the possible causes for these departures. The discussion will be divided as follows: (1) experimental and simulation agreement with measured acceleration-phase implosion characteristics; (2) effects of long-wavelength perturbations; (3) Rayleigh-Taylor unstable growth during the deceleration phase of the implosion; and (4) effects of Rayleigh-Taylor unstable growth during the acceleration phase of the implosion.

### Acceleration Phase Comparisons

The first area of agreement is between experiments and simulations of the (large-scale) dynamics of a glass-ablator capsule during the acceleration phase of the implosion. A series of experiments was conducted to determine a value for the electron thermal-conduction flux limiter.<sup>13</sup> The experiments examined the absorbed laser energy and the fraction of x rays emitted using solid glass targets. The absorbed laser energy was measured with a set of 15 plasma calorimeters symmetrically arranged about the target chamber; the energy re-emitted as x rays was determined by a single differential x-ray calorimeter. The flux limiter was adjusted in the simulations until good agreement between the predicted and observed values for the absorbed laser energy was obtained over the incident laser intensity range of  $\sim 10^{13}$ – $10^{15}$  W/cm<sup>2</sup>. The flux-limiter value giving the best agreement was  $f_e = 0.06$ . Using this value, the x-ray conversion data also showed good agreement over this same intensity range. The same value of  $f_e$ , when used to model imploding glass-ablator capsules, was found to give agreement between measurements and simulation for the absorbed-laser-energy fraction and x-ray-conversion efficiencies to within  $\pm 5\%$  over the same intensity range.

To further check our ability to simulate the coarse features of the hydrodynamic behavior during the acceleration phase, comparisons were made of the measured and predicted implosion time histories of glass-ablator capsules. These comparisons were carried out using a number of x-ray diagnostics. Figure 43.4 displays the implosion history of a 25-atm, D<sub>2</sub>-filled,  $\sim 5$ - $\mu\text{m}$ -thick glass-ablator capsule obtained using x-ray streak photography. To highlight the image structure, which is dominated by emission at the time of stagnation, two color cycles have been used on a nonlinear intensity scale. The solid lines, superimposed on the experimental image, show the *LILAC* prediction for the maximum-emission radius as a function of time. (Near the time of maximum compression, emission from the fuel core causes the calculated trajectory to jump to the axis.) Since the absolute timing was unknown on this shot, the relative timing between the experimental data and 1-D prediction has been adjusted to give the best fit. Up to the point of maximum compression, very good agreement exists between the experimental and predicted trajectories. However, after peak compression, departures can be noticed. The core is displaced (positive



E5272

Fig. 43.4  
 Implosion history of a 25-atm,  $D_2$ -gas-filled capsule recorded by an x-ray-imaging streak camera. The trajectory of maximum x-ray emission calculated using *LILAC* is superposed (solid line).

radius direction in Fig. 43.4) and the upper disassembly trajectory ( $r > 0$ , Fig. 43.4) is in better agreement with the simulation than for the lower trajectory. Additional comparisons between simulations and experiments were made using the results obtained from an x-ray-framing camera.<sup>16–18</sup> The framing camera consisted of a pinhole camera assembly with an array of pinholes illuminating a gated microchannel plate. For the results shown here, the framing time was  $\sim 150$ -ps FWHM and the time between frames was  $\sim 250$  ps. Figure 43.5 illustrates the agreement observed on cryogenic implosions for capsules of three different ablator thicknesses. Since no timing fiducial existed on the framing camera, the location of the first frame was selected to give the best agreement between experiment and simulation. Because the frame separation time is known, the placement of the remaining three frames is set by the location of the first. Figure 43.5 shows good agreement during the acceleration phase between simulation and experiment for the three ablator thicknesses.

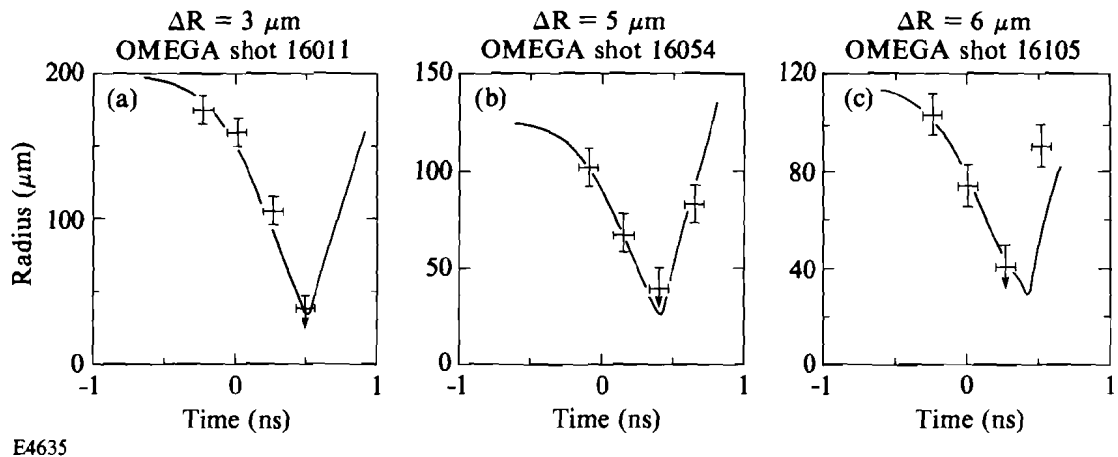


Fig. 43.5

Radius of peak x-ray emission versus time determined from framed x-ray images for three cryogenic capsules having (a) 3- $\mu\text{m}$ , (b) 5- $\mu\text{m}$ , and (c) 6- $\mu\text{m}$  initial ablator thickness. *LILAC* predictions of the same implosions are shown as solid lines. Times are with respect to the peak of the laser pulse.

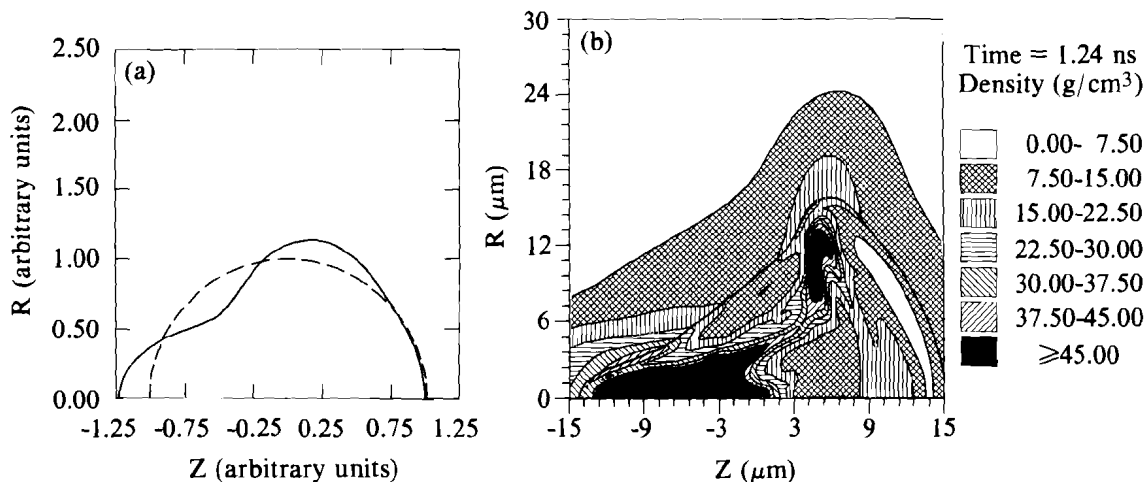
The comparisons of absorbed laser energy, x-ray energy conversion, and implosion time history (using  $f_e = 0.06$ ) show that our numerical simulations are able to predict the coarse features of the dynamic of imploding glass-ablator capsules during the acceleration phase. This implies that no large discrepancies exist between simulation and experiments on the energy amount available in the shell to compress and heat the fuel during the final stages of the implosion.

Having found agreement between the experiments and code predictions during the acceleration phase of the implosion, we now address issues that could result in the observed departures of the neutron yield and fuel areal density from 1-D predictions. These possible causes for departure cannot be quantitatively measured, except for their influence on the final core conditions, using diagnostics currently available on the OMEGA system.

### Long-Wavelength Perturbations

The presence of long-wavelength perturbations during the capsule implosion represents a possible source of disagreement between experiment and calculations. These long-wavelength perturbations were predominantly from variations in the frozen-fuel-layer thickness and laser power imbalance between the individual laser beams. Three sources of power imbalance have been identified for the OMEGA laser system.<sup>19</sup> The first arises from the state of polarization in each beam as it enters its third-harmonic conversion crystal, the second involves energy balance. The third source depends on the flux levels in each of the OMEGA laser amplifiers. Each of the sources modifies the shape of the laser pulse, resulting in the potential for long-wavelength ( $\ell \leq 4$ ) modes of on-target illumination nonuniformity whose amplitude as well as modal content can change in time. Simulations

of experiments conducted only with DPP's showed that power imbalances, of the types discussed above, may have resulted in on-target illumination nonuniformities of  $\sim 40\%$  peak-to-valley, in modes  $1 \leq \ell \leq 4$ , during the early portion of the implosion. (Between the DPP and SSD series of cryogenic implosion experiments the first two sources of power imbalance were improved on OMEGA. Work is still underway on the third source at this time.) Two-dimensional (2-D) *ORCHID* simulations have shown that these levels of long-wavelength illumination nonuniformity would dominate the possible effects of the measured,  $\ell \leq 2$ , fuel-layer-thickness variations. To examine a "worst-case" situation, a 2-D simulation was carried out for which the level of illumination nonuniformity in modes  $1 \leq \ell \leq 4$  was held fixed at 45% peak-to-valley over the duration of the laser pulse. Figure 43.6 displays the predicted fuel density of the imploded core at the time at which the simulated yield equals the measured yield for pellets of similar initial ablator thickness ( $\sim 5 \mu\text{m}$ ). Note that although only long-wavelength modes were initially applied, their nonlinear interactions during the final implosion stages have resulted in the generation of shorter-wavelength distortions in the fuel region. (When the same modes were applied with a peak-to-valley variation of only 10%, the strong mode-mode interactions were not observed; a Legendre decomposition of the fuel  $\rho R$  showed that the dominant distortions remained.)



TC2549

Fig. 43.6

Two-dimensional (*ORCHID*) hydrodynamic simulation of a 5- $\mu\text{m}$ -glass-ablator cryogenic implosion subjected to long-wavelength illumination nonuniformities.

- Illumination-nonuniformity pattern placed on target (solid line), modes  $1 \leq \ell \leq 4$ , peak-to-valley of  $\sim 45\%$ .
- Density contours ( $\text{g}/\text{cm}^3$ ) at the time when the simulation yield equaled the level of experimentally observed yield for similar-ablator-thickness capsules.

The 2-D simulations show that the predicted overall effect on cryogenic capsule performance of long-wavelength nonuniformities is a reduction of neutron yield by a factor of 2 to 10 for peak-to-valley variations in the 10%-to-45% range in modes  $1 \leq \ell \leq 4$ . This yield reduction is due to a lower efficiency of kinetic-to-internal energy conversion during the stagnation phase of the implosion. The neutron-weighted fuel areal density, while aspherical, is not appreciably changed from simulations carried out assuming perfect illumination uniformity. Depending on the modal content of the perturbation, the neutron-weighted  $\rho R_f$  could be reduced due to an increased final fuel volume from the uniform case. However, in some cases, the  $\rho R_f$  could also increase due to both cooler core conditions and a temporal shift of the neutron production such that the  $\rho R_f$  is weighted toward a time when high fuel densities are present. (If all of the 45% peak-to-valley were placed in a pure  $\ell = 2$ , the effect on capsule performance would have been more substantial, especially with respect to the fuel areal density. However, numerical simulations of the potential power imbalance present on the OMEGA system during the DPP-only series show that the concentration of a majority of the resulting illumination nonuniformity in an  $\ell = 2$  mode was highly unlikely.)

### Rayleigh-Taylor Unstable Growth

The simulations in the previous section do not take into account the potential effects of fuel-ablator mixing during the deceleration (stagnation) phase of the implosion. Two possible sources could result in mixing of fuel and ablator material. For long-wavelength cases (see Fig. 43.6), mixing could occur due to shear and/or vortex-like flows that develop near the fuel-ablator interface. A second source of mixing could be driven by the development of Rayleigh-Taylor<sup>17,18</sup> unstable flow and convergence effects during the deceleration stage of the implosion.

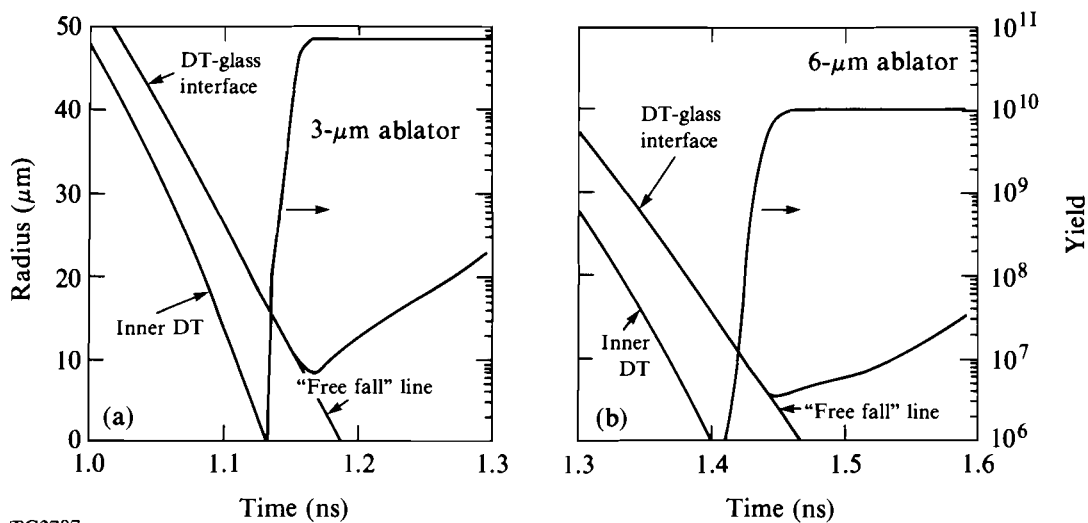
For long-wavelength modes, *ORCHID* simulations show that while shear and vorticity-generated vortex flows would result in mixing of ablator and fuel material, the time and spatial scale of this mixing would not fully explain the experiments. The *ORCHID* simulations show that over ~90% of the neutron yield should be obtained before strong shear and vortex flows develop to any large extent. Therefore, since the simulation in Fig. 43.6 represents a “worst” case, we do not believe that long-wavelength perturbations explain the differences between experiment and simulation.

The potential effects of short-wavelength Rayleigh-Taylor instabilities during the deceleration phase of the implosion have been examined. One- and two-dimensional simulations have shown that there are two regions where Rayleigh-Taylor unstable flow should develop. The first region is a DT-DT “interface” between the hotter inner fuel and the surrounding colder fuel; the second is the fuel-ablator interface. *ORCHID* simulations of single modes (run in the small-amplitude, linear regime) show that both of these regions have essentially “classical” Rayleigh-Taylor growth rates, which can be approximated by the expression<sup>20</sup>

$$\gamma \approx \sqrt{A(t)kg(t)/[1 + kL(t)]}, \tag{1}$$

where  $A(t)$  is the Atwood number,  $k$  is the unstable wave number,  $g(t)$  is the acceleration, and  $L(t)$  is a density scale length. The potential growth of all unstable modes and the subsequent mixing at the DT-DT unstable region, while possibly resulting in a neutron-yield reduction due to lower kinetic energy to thermal energy conversion, would not explain the observed reductions in fuel areal density and might, in some situations, result in higher  $\rho R_f$  due to the cooling of the hotter DT region.

Mixing of fuel and ablator material due to unstable growth at the ablator-fuel interface has been examined using a simplified model. This model shows that while mixing of fuel and ablator material could potentially take place, the time and spatial scales are again insufficient to explain the departures in capsule performance. This can be seen by an analysis of the “free fall” trajectory of shell material into the fuel. The maximum penetration rate of ablator material into the fuel during the stagnation phase of the implosion is given by the glass-shell velocity at the fuel-glass interface at the time the shell begins to decelerate (assuming that no external forces act on the ablator material). Assuming the neutron production in a given zone is stopped as the free fall trajectory passes through that fuel zone, one can estimate the yield reduction that might take place due to mixing. Figures 43.7(a) and 43.7(b) show the results of this calculation for a 3- $\mu\text{m}$  and a 6- $\mu\text{m}$  ablator thickness. For these cases, essentially all of the yield occurs before mixing can quench it.



TC2787

Fig. 43.7  
 Radial location of the inner fuel edge, fuel-ablator interface, “free-fall” trajectory, and neutron yield (right-hand axis) versus time for a (a) 3- $\mu\text{m}$ -glass-ablator and (b) 6- $\mu\text{m}$ -glass-ablator cryogenic capsule implosion.

The effect of Rayleigh-Taylor unstable growth during the acceleration phase of the implosion was the last area to be examined. One- and two-dimensional simulations have shown a number of potential Rayleigh-Taylor unstable regions present during the acceleration phase of the glass-ablator cryogenic capsules. Figure 43.8 displays the pressure and density profiles at various times for an implosion using a 3- $\mu\text{m}$ -thick ablator. Figure 43.8 shows that there are two unstable regions present during the acceleration phase. The first is located at the electron thermal-conduction-driven ablation surface, while the second is located within the DT fuel itself. (The unstable region in the DT is caused by the large differences in equation of state and opacities for DT and glass.) Two-dimensional *ORCHID* simulations of single-wavelength perturbations, calculated well within the small-amplitude, linear-growth region have shown that the Rayleigh-Taylor growth rates at the electron thermal-conduction-driven ablation surface can be approximated as

$$\gamma \approx \sqrt{A(t)kg(t)/[1 + kL(t)]} - \beta kV_a(t), \quad (2)$$

where  $V_a(t)$  is the ablation velocity and  $\beta$  is a constant that can range between 1 and 3 depending on the definitions used for  $A(t)$ ,  $L(t)$ , and  $V_a(t)$ . *ORCHID* simulations show that the DT unstable interface is essentially “classical” modified by a small density-scale-length [ $L(t)$ ] term [Eq. (1)]. When the ablator thickness becomes greater than  $\sim 4.5 \mu\text{m}$ , the simulations show that the situation, in terms of unstable interfaces, becomes more complicated. An additional unstable region evolves in the ablator associated with a radiation wave propagating into it. This feature is illustrated in Fig. 43.9 for an initially 5- $\mu\text{m}$ -thick ablator. Two-dimensional simulations show that the unstable growth rates of this surface are greater than those of the electron thermal-conduction ablation surface but lower than the DT unstable region.

A modal analysis stability model similar to the one presented in Ref. 21 was used to examine the potential effects of all these unstable regions on pellet performance. *ORCHID* was run in the small amplitude linear region to determine the growth-rate spectrum for all the unstable regions for a given pellet implosion. These growth rates were then incorporated into the stability model to determine the potential amount of mix that could occur during the acceleration phase. The results show that the development of the DT unstable region plays the dominant role in these implosions. For capsules with initial ablator thickness  $\geq 4.5 \mu\text{m}$ , the unstable region associated with the radiation wave is also important. However, for all ablator thicknesses considered, the model indicates that the growth at the DT unstable interface alone could result in substantial mixing of the DT fuel with ablator material during the acceleration phase.

Currently the multidimensional programs used for ICF implosion simulations are incapable of modeling all of the unstable modes of interest during an implosion. However, to at least determine if this unstable behavior could be the potential source for mixing during the acceleration

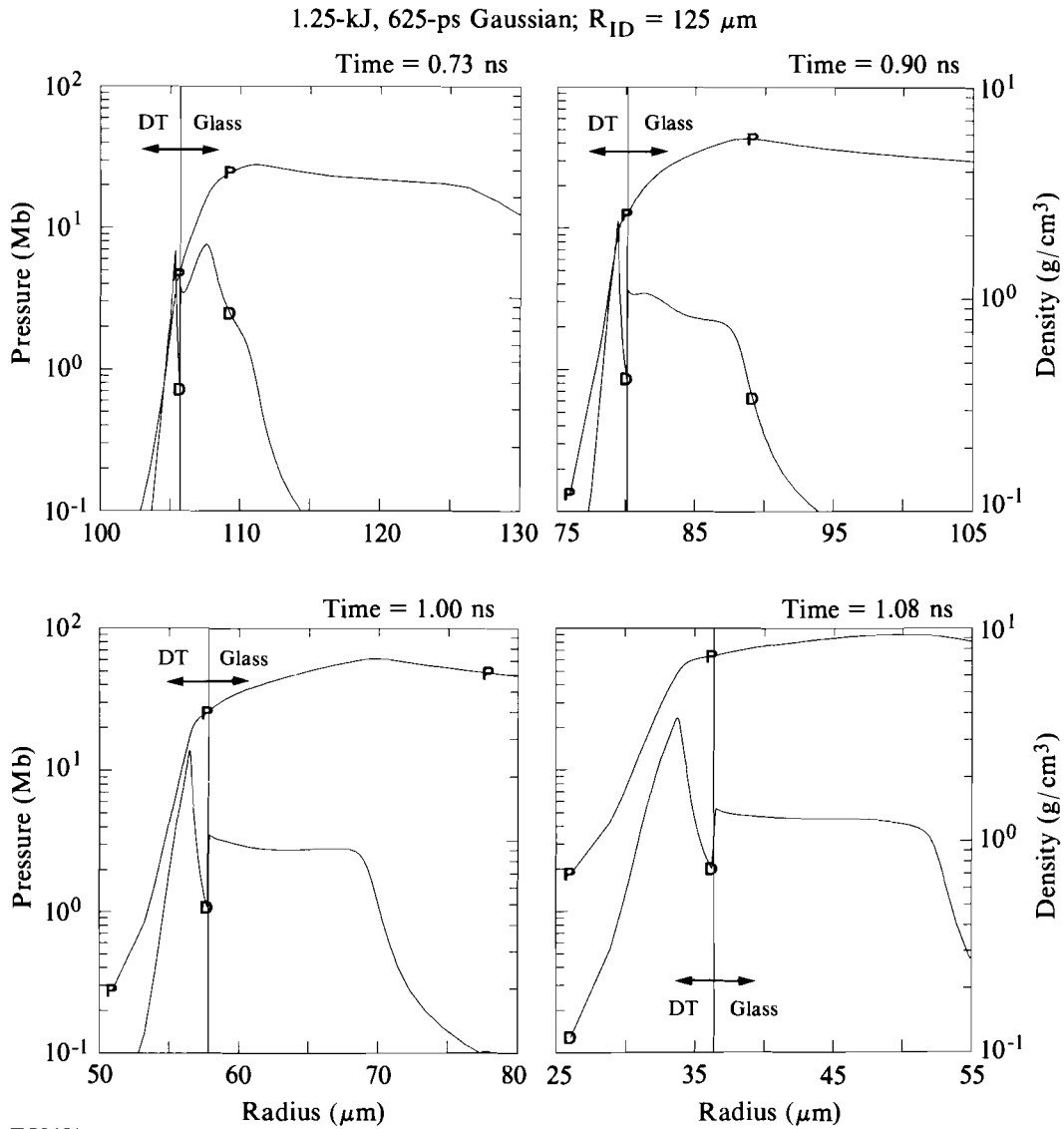
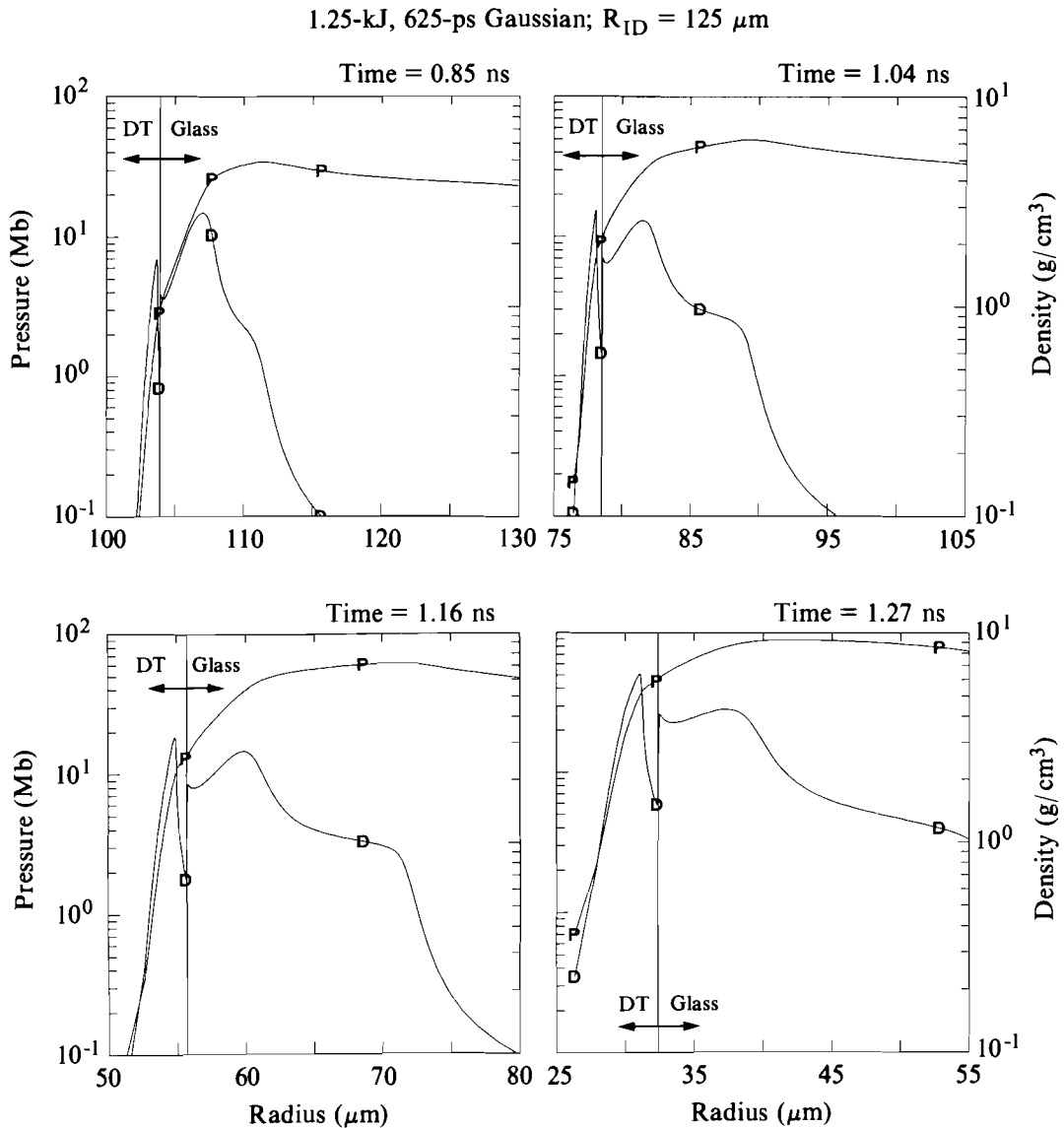


Fig. 43.8 Pressure and density profiles versus radius at various times for a 3- $\mu\text{m}$ -glass-ablator cryogenic capsule implosion.

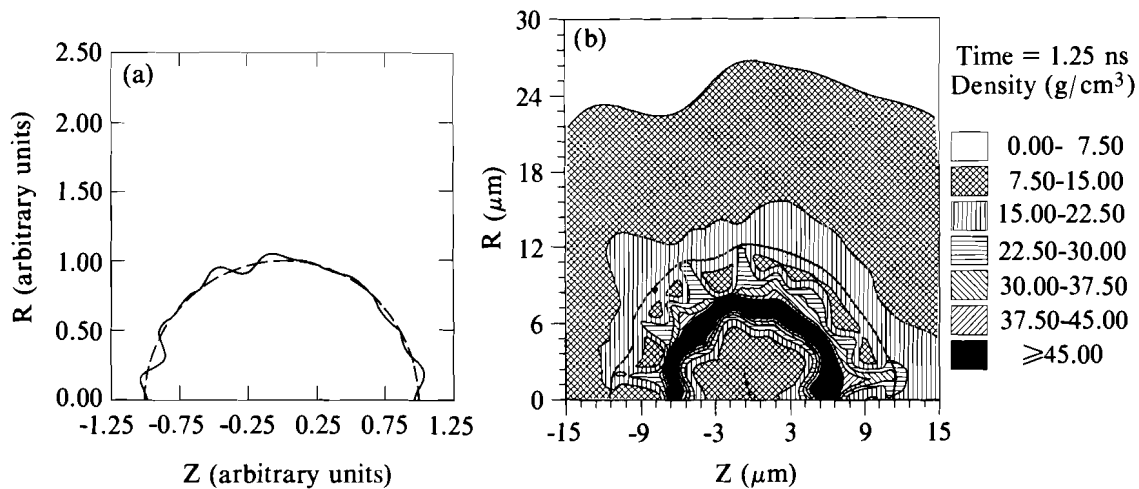
phase, a two-dimensional *ORCHID* simulation was conducted that considered the modes  $2 \leq \ell \leq 20$  with a total illumination nonuniformity of  $\sim 15\%$  peak-to-valley. Assuming DPP illumination only, this represents the illumination-nonuniformity level predicted (in these modes). Figure 43.10 displays the density conditions of the pellet at the time when the experimental and simulation yield are equal. The large distortions present at an average radius of 9  $\mu\text{m}$  are due to the development of the DT unstable region during the acceleration phase. The seeds for this growth were transmitted from



TC2652

Fig. 43.9 Pressure and density profiles versus radius at various times for a 5- $\mu\text{m}$ -glass-ablator cryogenic capsule implosion.

nonuniformities at the ablation surface during the implosion. The simulation shows that this surface has undergone a large amount of distortion and has resulted in mixing of fuel and ablator material before deceleration. Due to the limited number of modes considered, the mixing in this simulation is confined to the outer region of the fuel, and the calculated yield reduction is small, approximately a factor of 10 below the uniform illumination simulation.



TC2551

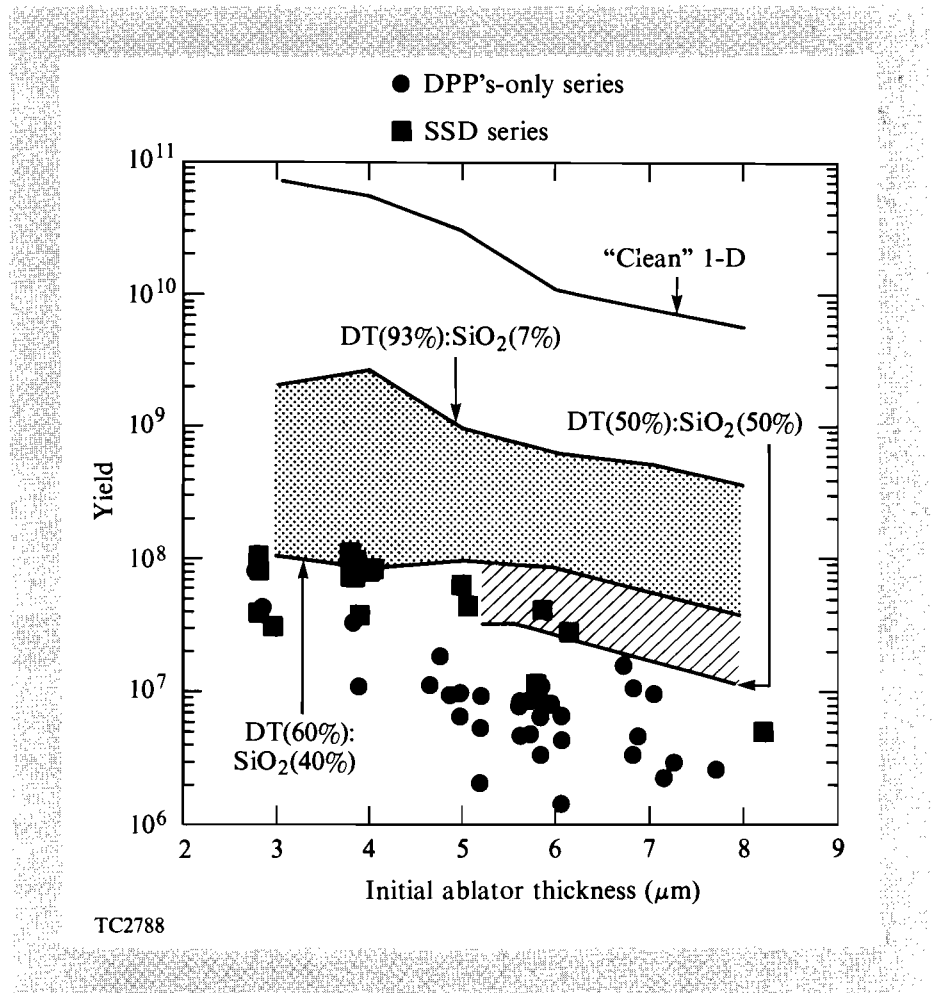
Fig. 43.10

Two-dimensional (*ORCHID*) hydrodynamic simulation of a 5- $\mu\text{m}$ -glass-ablator cryogenic implosion subjected to illumination nonuniformities in modes  $2 \leq \ell \leq 20$ .

- Illumination-nonuniformity pattern placed on target (solid lines) modes  $2 \leq \ell \leq 20$  with a total peak-to-valley of  $\sim 15\%$ .
- Density contours ( $\text{g}/\text{cm}^3$ ) at the time when the simulation yield equaled the level of experimental observed yield for similar-ablator-thickness capsules.

The modal analysis modeling, incorporating modes  $\ell \leq 500$ , indicates that the DT layer could be mixed with the ablator material and very early in the implosion. Because the mixing is predicted to take place early in the implosion, several 1-D pre-mixed simulations were conducted to examine the potential consequences of this mixing on pellet performance. The premixed simulations assume that initially a certain fraction of the inner glass-ablator material is uniformly distributed into the DT fuel.

Figure 43.11 shows the measured neutron yields and the 1-D results of the premixed simulations for several  $\text{SiO}_2$ -to-DT mix ratios. The results for the measured and calculated neutron-weighted fuel areal density are shown in Fig. 43.12. The yield results (see Fig. 43.11) show that the mixing of ablator material with the DT during the acceleration phase of the implosion has a large influence on the neutron yield. These simulations do not take into account energy associated with mixing during the stagnation phase and neglect the effects of the other sources of potential departure from one-dimensional behavior discussed previously. For example, 2-D simulations of the effects of long-wavelength modes on the premixed implosions show additional yield reductions of 2 to 10, depending on the illumination-nonuniformity level. Therefore, combining the dominant effect of acceleration mixing of DT and ablator with long-wavelength-modes effects,



TC2788

Fig. 43.11  
Observed yields and one-dimensional hydrodynamic simulation yields assuming a number of DT-to-SiO<sub>2</sub> fuel (pre-mixed) mix ratios versus initial ablator thickness.

results in yields consistent with those observed in the experiments. Figure 43.12 shows that the predicted fuel areal densities from the premixed simulations bracket the values of  $\rho R_f$  observed experimentally.

Of course, these mix estimates are *ad hoc*. Currently it is impossible to define a unique level of mixing that must have taken place during these implosions. A detailed knowledge of the contributions of long-wavelength modes and the source and levels of perturbations at the unstable regions would be required for such a calculation. We have assumed that the perturbations at the fuel-ablator interface region were the result of feed-through of drive nonuniformities from the ablation surface. However, the inside-surface finish of the glass targets and potential early nonuniform “freeze out” of high-*Z* contaminants in the DT fuel could also act as initial perturbations at the DT-ablator interface. These sources of initial perturbations can vary from capsule to capsule. However, assuming mixing

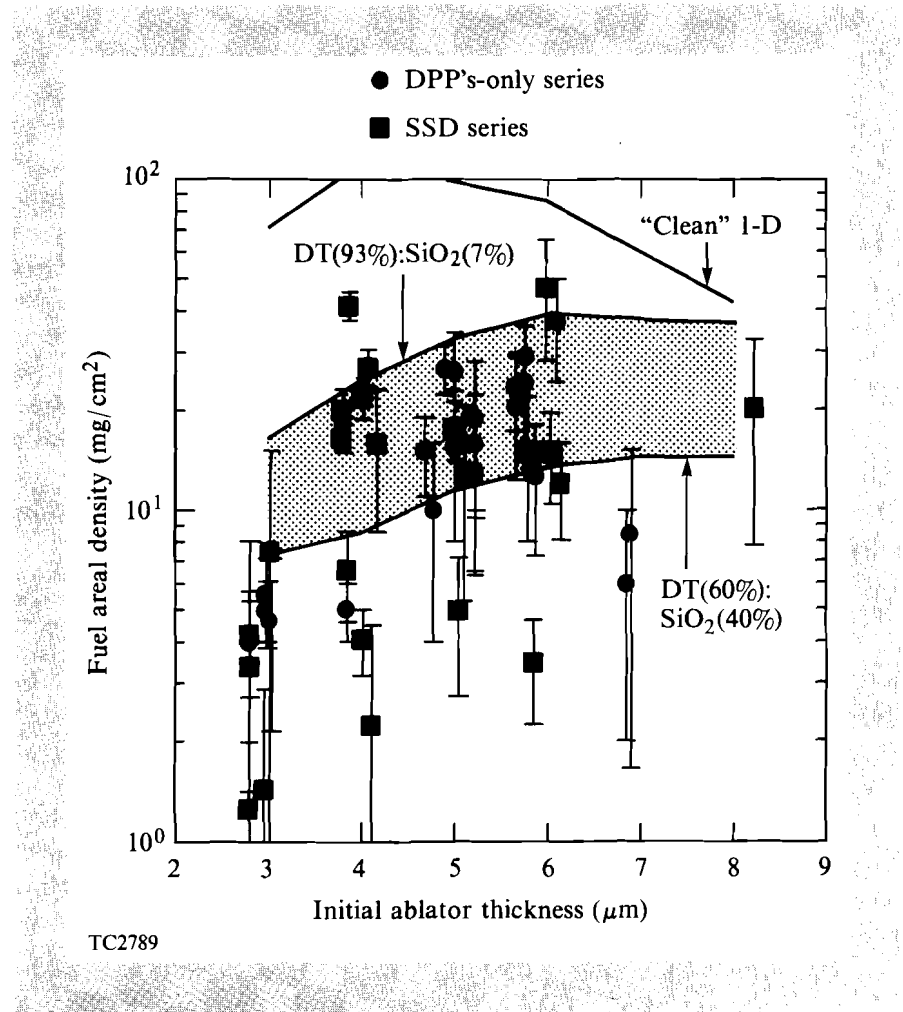


Fig. 43.12  
 Measured fuel areal densities and one-dimensional predicted fuel areal densities assuming a number of DT-to-SiO<sub>2</sub> fuel (pre-mixed) mix ratios versus initial ablator thickness.

ratios higher than about 50% DT:50% SiO<sub>2</sub> does not appear plausible because the predicted fuel areal density would be much lower than that observed experimentally (see Fig. 43.12).

This study has identified that the classically unstable interface within the DT, and subsequent mixing with ablator material during the acceleration phase, could be the dominant contributor to the observed departures between glass-ablator cryogenic-implosion experimental results and simulation predictions. (Unstable flow development in the ablator becomes increasingly important as the initial ablator thickness increases.) The classical Rayleigh-Taylor growth rates, in conjunction with the thinness ( $\leq 5 \mu\text{m}$ ) of the cryogenic fuel layer during the acceleration phase, place severe constraints on required levels of illumination uniformity and the finish of the fuel-glass interface.

Proposed high-gain direct-drive capsule designs have been planned to eliminate the occurrence of a classical growth Rayleigh-Taylor unstable region in the fuel layer near the ablator-fuel interface by using low-atomic-number ablators and pulse shaping. Experiments planned for OMEGA will begin to address the hydrodynamic behavior of capsules more closely related to the proposed high-gain designs. This study will be carried out in three broad stages. The first stage will examine the hydrodynamic behavior during the acceleration phase of low-atomic-number ablator capsules. The second stage will use noncryogenic "surrogate" cryogenic capsules to examine the dynamics of a hydrodynamically equivalent, surrogate cryogenic capsule implosion. Finally, upon successful completion of the first two stages, cryogenic-capsule implosions using low-atomic-number ablators will be conducted. This phase in the experiments will require advances in target-fabrication techniques since the initial fuel-layer thickness will be of the order of 20 to 30  $\mu\text{m}$ .

#### ACKNOWLEDGMENT

This work was supported by the U.S. Department of Energy Division of Inertial Fusion under agreement No. DE-FC03-85DP40200 and by the Laser Fusion Feasibility Project at the Laboratory for Laser Energetics, which has the following sponsors: Empire State Electric Energy Research Corporation, New York State Energy Research and Development Authority, Ontario Hydro, and the University of Rochester.

#### REFERENCES

1. F. J. Marshall, S. A. Letzring, C. P. Verdon, S. Skupsky, R. L. Keck, J. P. Knauer, R. L. Kremens, D. K. Bradley, T. Kessler, J. Delettrez, H. Kim, J. M. Soures, and R. L. McCrory, *Phys. Rev. A* **40**, 2547 (1989).
2. R. L. McCrory, J. M. Soures, C. P. Verdon, F. J. Marshall, S. A. Letzring, S. Skupsky, T. J. Kessler, R. L. Kremens, J. P. Knauer, H. Kim, J. Delettrez, R. L. Keck, and D. K. Bradley, *Nature* **335**, 225 (1988).
3. G. Taylor, *Proc. R. Soc. London Ser. A* **201**, 192 (1950).
4. D. J. Lewis, *Proc. R. Soc. London Ser. A* **202**, 81 (1950).
5. S. Chandrasekhar, *Hydrodynamic and Hydromagnetic Stability* (Clarendon Press, Oxford, England, 1961), Chap. 10.
6. LLE Review **33**, 1 (1987).
7. S. Skupsky, R. W. Short, T. Kessler, R. S. Craxton, S. Letzring, and J. M. Soures, *J. Appl. Phys.* **66**, 3456 (1989).
8. B. I. Bennett, J. D. Johnson, G. I. Kerley, and G. T. Rood, Los Alamos National Laboratory Report LA-7130 (1978).
9. W. F. Huebner, A. L. Merts, N. H. Magee, Jr., and M. F. Argo, Los Alamos National Laboratory Report LA-6760-M (1977).
10. M. Born and E. Wolf, *Principles of Optics* (Pergamon, New York, 1975), p. 123.